CHEMISTRY OF MATERIALS
Cite This: Chem. Mater. 2019, 31, 8839−8849
Article
pubs.acs.org/cm

$K_2Ge_3As_3$: Fiberlike Crystals of a Narrow-Band-Gap *Zintl* Phase with a One-Dimensional Substructure $^1_\infty\{(Ge_3As_3)^{2-}\}$

Armin R. Eulenstein,[†] Dimitri Bogdanovski,[‡] Hendrik Reinhardt,[†] Vanessa Miß,[†] Bernhard Roling,[†] Norbert Hampp,[†] Richard Dronskowski,[‡,§] and Stefanie Dehnen*[,†]

[†]Fachbereich Chemie und Wissenschaftliches Zentrum für Materialwissenschaften, Philipps-Universität Marburg, Hans-Meerwein-Straße 4, 35043 Marburg, Germany

[‡]Chair of Solid-State and Quantum Chemistry, Institute of Inorganic Chemistry, RWTH Aachen University, Landoltweg 1, D-52056 Aachen, Germany

[§]Hoffmann Institute of Advanced Materials, Shenzhen Polytechnic, 7098 Liuxian Blvd, Nanshan District, 518055 Shenzhen, China

Supporting Information

ABSTRACT: The novel ternary phase $K_2Ge_3As_3$ was prepared by fusion of the elements. It crystallizes in very thin, deeply black fibers exhibiting metallic luster. The appearance is in accordance with its crystal structure that comprises an unprecedented one-dimensional anionic substructure, $^1_\infty\{(Ge_3As_3)^{2-}\}$, and it reflects its optical absorption properties. Both an experimental UV−visible spectrum and density-functional theory (DFT)-based band structure calculations hint toward a narrow-band-gap semiconductor. The band gap obtained from DFT using the SCAN functional is approximately 1.4 eV, in excellent agreement with the experimental data. We present the synthesis, structure, electronic properties, and bonding character of this new *Zintl* phase. Impedance spectroscopy reveals similar electronic and ionic conductivity of the phase.

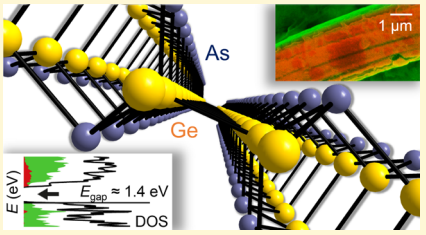

INTRODUCTION

Multinary alloys are very promising materials, the properties of which can be subtly modified, hence "fine-tuned", by the choice of the (semi)metals used for their synthesis. Upon usage of one s-block and two p-block elements for the formation of ternary compounds, the two p-block (semi)-metals tend to form bimetallic anions that belong to the class of *Zintl* anions. In recent times, *Zintl* phases like Mg_3Sb_2, Sr_3GaSb_3, Ca_3AlSb_3, $Ca_5Al_2Sb_6$, or $Yb_{14}MnSb_{11}$ have attracted attention as new thermoelectric materials,[1−10] as they possess structural characteristics that are beneficial for electron-crystal phonon-glass properties that result in high thermoelectric efficiencies. Other *Zintl* compounds like $Eu_{14}MnSb_{11}$, $EuIn_2As_2$, MgB_2, $Ba_2Sn_3Sb_6$, or $SrSn_3Sb_4$ were reported to feature colossal magnetoresistance[11,12] or superconductivity.[13,14] The dimensionality of the anionic substructures in the respective solids varies from molecular (zero-dimensional) and low-dimensional (one-dimensional, 1D) structures to layered (two-dimensional, 2D) or extended (three-dimensional, 3D) anionic networks. However, anisotropic structural features (1D, 2D), which may cause anisotropic physical properties, were usually not macroscopically reflected in the morphology of the single crystals.

Irrespective of the dimensionality of the underlying solid-state compound, many of these compounds have furthermore been used in the recent past for the preparation of soluble salts of molecular binary *Zintl* anions.[15−20] The latter are of great interest as precursors for the targeted synthesis of ternary intermetalloid clusters,[15,21−25] which we have intensively studied over the past years regarding their synthesis and formation mechanisms and, finally, the chemical and physical properties of multimetallic particles. As many of the ternary phase diagrams of A/E′/E″ (A = alkali metal, E′, E″ = elements from groups 13, 14, and 15, respectively) are still unknown, most of the mentioned salts were formed in an explorative manner by permutation of the compositions of the ternary mixtures to improve purities and yields. We could recently show that the compositions of the underlying mixtures often deviate from the actual target composition. The compound $[K(crypt\text{-}222)]_2[TlBi_3]$, for instance, is preferably prepared from a solid compound based on a 1D-anionic substructure, K_2TlBi, which is the main component of an as-prepared ternary 5:2:4 solid mixture; fusing of the elements in a 2:1:1 ratio, however, yields the solid compound $K_6Tl_2Bi_3$ as the main product.[26] Similar observations were made for elemental combinations A/Tt/Pn (Tt = tetrel = group 14 element; Pn = pentel = group 15 element): for the preparation of the salts $[K(crypt\text{-}222)]_2[Tt_2Pn_2]$, being isoelectronic to $[K(crypt\text{-}222)]_2[TlBi_3]$, best results in terms of purity and yield are also obtained upon extraction of solids with the nominal composition A_2TtPn, with some exceptions, in which alternate stoichiometries $A_2Tt_2Pn_2$ or $A_2E_{14}E_2$[15] work better.[26]

Received: July 16, 2019
Revised: September 23, 2019
Published: September 24, 2019

DOI: 10.1021/acs.chemmater.9b02827
Chem. Mater. 2019, 31, 8839−8849

To improve the knowledge about such ternary mixtures and the chemical phases in them, we are currently expanding our work, especially focusing on Tr/Tt combinations (Tr = triel, group 13 element) that involve two p-block semimetals.

In this report, we present and discuss our most recent result obtained in the system K/Ge/As. Controlled thermal treatment of an as-prepared solid of the nominal composition "K_2GeAs_2"[27] led to the crystallization of a solid with the composition $K_2Ge_3As_3$ (**1**). The unprecedented one-dimensional anionic structure of **1** is accompanied by an intriguing anisotropic, fiberlike morphology, which prompted us to investigate this new compound in detail. Indeed, the crystal structure of **1** may be viewed as the result of a dimensional reduction from the related, known solid KGe_3As_3:[28] the latter is based on a 2D-anionic structure, which is cleaved into strands by addition of another equivalent of reducing potassium. Both compounds are structurally related to the binary phase $GeAs_2$.[29,30]

EXPERIMENTAL SECTION

Synthesis. All synthetic steps were performed under strict exclusion of air and moisture in a dry Ar atmosphere using standard Schlenk or glovebox techniques. $K_2Ge_3As_3$ (**1**) was prepared in a two-step synthesis. Step 1: The elements are weighed in a 2K:Ge:2As ratio, placed in a silica tube, molten, and heated up to yellow heat by means of an oxygen/methane torch until a homogeneous melt is observed. This process takes around 15 mins. Care has to be taken during the initial, highly exothermic reaction between K and Ge/As. The mixture is allowed to slowly cool down by gradually reducing the amount of oxygen in the flame. At room temperature, one obtains a very hard solid exhibiting a metallic luster of a so-far unknown composition, which is then ground into a fine powder within an Ar-filled glovebox. The corresponding powder X-ray diffraction pattern indicates the presence of a complex mixture of phases, yet containing neither compound **1** nor any of the known binary or ternary solids, GeAs,[31,32] $GeAs_2$,[29,30] K_4Ge_9,[33] K_3As_7,[34] K_3As_{11},[35] K_2GeAs_2,[27] KGe_3As_3,[28] nor the elements (Figures S5 and S6). Apparently, in the absence of a tempering step, kinetic control of the reaction takes place that allows for the formation of an unknown, metastable phase. A thermogravimetric analysis and differential scanning calorimetry (TGA/DSC) measurement of this mixture showed a steep decline in mass and an exothermic reaction of this crude product setting in at around 750 °C (Figure S4). Step 2: The as-prepared powder is transferred into an open corundum crucible and placed in a silica tube. After evacuation of the tube, the temperature profile depicted in Figure S1 is applied to the sample with a maximum temperature of 750 °C. **1** is formed as an air- and moisture-sensitive fibrous material with a metallic luster, which grows on top of the corundum crucible upon slow cooling in the range between 750 and 500 °C (Figure 1).

During the tempering process, **1** is separated from excess Ge and As owing to the temperature gradient within the tube furnace. Ge is found at the formerly hottest part of the tube, followed by **1** along the temperature gradient. Excess As condenses at the coldest part of the tube. In a typical laboratory setup, we obtained around 1.5 g of **1**, which can be scaled up easily, being only limited by the size of the ampoule and the furnace. The phase purity of compound **1** was confirmed by powder X-ray diffraction (Figure S7). With its K:Ge:As = 2:3:3 composition, the new compound **1** is closest to an equimolar mixture of elements in the ternary system K/Ge/As (see Scheme 1).

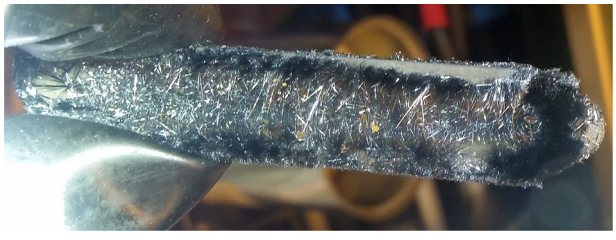

Figure 1. Single crystals of **1** grown on the walls of a corundum crucible.

Scheme 1. Diagram of the Ternary System K/Ge/As[a]

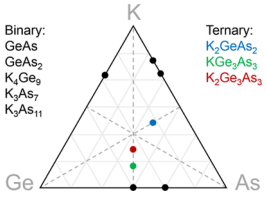

[a]The colored circles represent the compositions of the known ternary compounds K_2GeAs_2,[27] KGe_3As_3,[28] and $K_2Ge_3As_3$ (**1**; this work), which are named in the scheme in corresponding colors. For completeness, we also indicate (black circles) the compositions of the known binary solids GeAs and[31,32] $GeAs_2$,[29,30] as well as the compositions of the binary *Zintl* phases K_4Ge_9,[33] K_3As_7,[34] and K_3As_{11}.[35]

Powder X-ray Diffraction. Powder X-ray diffraction patterns of **1** were measured on a Stoe StadiMP diffractometer system equipped with a Mythen 1 K silicon strip detector and a Cu Kα (λ = 1.54056 Å) radiation source. Crystals of **1** were filled into a glass capillary (0.3 mm diameter), which was then sealed air-tight with soft wax. The tube was then mounted onto the goniometer head using wax (horizontal setup) and rotated throughout the measurement.

Thermogravimetric Analysis and Differential Scanning Calorimetry. TGA/DSC measurements were performed with a Netzsch STA 409 CD instrument in in aluminum oxide crucibles, with an argon flow rate of 40 mL min^{-1} and a heating rate of 1 K min^{-1}.

Single-Crystal X-ray Diffraction. Because of the tendency of **1** to defiber on touch, a suitable bundle of parallel oriented fibers was selected and cut on one side to obtain a short enough piece to be completely immersed into the X-ray beam. Splicing of the fibers at the cutting point led to some spot separation in the final diffraction images. This effect was overcome by choosing a sufficiently large integration mask and integrating the slightly separated peaks as one. The data for the X-ray structural analyses were collected at T = 100(2) K with Mo Kα-radiation ($\lambda_{\text{Mo K}\alpha}$ = 0.71073 Å) on an area detector system Stoe IPDS2. The structures were solved by direct methods (SHELXT from SHELXL-2018/1[36]) and refined by full-matrix least-squares methods against F^2 with the SHELXL program[37] within the same program package. The crystal data and details of the structure solution and refinement are collected in Table 1.

Micro X-ray Fluorescence Spectroscopy (μ-XRF). μ-XRF measurements were performed with a Bruker M4 Tornado spectrometer, equipped with an Rh-target X-ray tube and a silicon drift detector. The emitted fluorescence photons were detected with an acquisition time of 100 s. Quantification of the elements was achieved through deconvolution of the spectra.

Electron Microscopy. Electron micrographs of **1** were taken on a Jeol JSM 7500F scanning electron microscope at 10 kV acceleration voltage. Samples were prepared in an argon-filled glovebox by dropping **1** suspended in toluene onto carbon film-coated TEM grids (Cu, 300 mesh). This special type of preparation was chosen to reduce the background signal. Imaging was conducted by simultaneous signal acquisition from a secondary electron detector and a backscattered electron detector. The superposition of signals from both detectors provides information on morphological aspects in green color (SE-detector) and material contrast in orange color (BE-detector).

Ultrasonic Treatment. **1** (20 mg) was suspended in 10 mL of toluene and treated in an ultrasonic bath EMAG Emmi 60HC for up to 200 min at maximum intensity setting.

DOI: 10.1021/acs.chemmater.9b02827
Chem. Mater. 2019, 31, 8839−8849

Table 1. Crystal Data and Details of the Single-Crystal Structure Solution and Refinement of 1

empirical formula	$K_4Ge_6As_6$ (=2 $K_2Ge_3As_3$)
formula weight (g mol^{-1})	1041.46
crystal color and shape	black, thin fibers with a metallic luster
crystal dimensions (mm)	0.378 × 0.025 × 0.010
crystal system	orthorhombic
space group	*Pnnm* (no 58)
a (Å)	14.1466(7)
b (Å)	16.3002(10)
c (Å)	3.7489(2)
V (Å)	864.47(8)
Z, ρ_{calc} (g cm^{-3})	2, 4.002
μ ($Mo_{K\alpha}$) (mm^{-1})	22.627
absorption correction type	numerical
2θ range (°)	5.77−60.99
index ranges	$-19 \le h \ge 20$, $-23 \le k \ge 23$, $-4 \le l \ge 5$
total number of reflections	7476
number of unique reflections (R_{int})	1505 (0.899)
obs. reflections [$I > 2\sigma(I)$]	1136
parameters	49
R_1 [$I > 2\sigma(I)$] / wR_2 (all data)	0.0526/0.1521
GooF (all data)	1.047
max peak/hole, (e Å^{-3})	1.70/−2.37

UV−visible Spectroscopy. UV−visible spectra were recorded with a Varian Cary 5000 dual-beam spectrometer equipped with a Praying Mantis sample holder from Harrik. The diffuse reflection of powdered samples was analyzed. The diffuse reflectance data was converted to an absorption spectrum by plotting $\lg(I_0/I_{diffuse})$ versus energy (eV).[38] Note that excessively vigorous grounding of the single crystals seems to lead to thermal decomposition of the compound, thereby leading to arbitrary spectra. Thus, the crystals were ground finely, yet carefully, to produce reproducible spectra with a sharp onset of absorption at the band-gap energy.

Computational Methodology. Quantum-chemical calculations based on density-functional theory (DFT) were performed utilizing the Vienna ab initio simulation package (version 5.4.4).[39−42] In all calculations, the projector-augmented wave (PAW)[43,44] method was employed for basis set representation, with the energetic cutoff set to 500 eV. For the initial structural optimization and calculation of the electronic properties, the generalized gradient approximation (GGA) functional in the parametrization of Perdew, Burke, and Ernzerhof[45] was chosen to account for electronic exchange and correlation effects. Brillouin zone integration was performed using Blöchl's tetrahedron method[46] for a Γ-centered **k**-mesh with dimensions of 4 × 4 × 14 to ensure energetic convergence. The valence electronic configurations of the individual species as given in the atomic potential files were $4s^13p^6$ for K, $4s^24p^2$ for Ge, and $4s^24p^3$ for As; a comparative calculation considering the 3d orbitals for Ge and As did not show any significant, observable effects in relation to electronic structure and bonding. The electronic convergence criterion was set to $\Delta E_{el} = 10^{-7}$ eV in relation to the total energy, whereas for structural optimization, the interatomic forces were minimized to less than 1 meV Å^{-1}. All calculations were performed without spin polarization.

Standard DFT functionals are prone to significant errors in describing excited-state properties, such as band-gap sizes, as is well known from the literature.[47−49] Thus, after the aforementioned optimization and a first evaluation of the electronic properties, a static calculation using the strongly constrained meta-GGA SCAN[50,51] functional was performed for the optimized structural model for increased accuracy in relation to the electronic structure. The wave function obtained from this calculation was projected onto atomic orbitals utilizing the LOBSTER program[52−55] to extract local properties from the delocalized PAW basis sets, yielding complete accuracy for the partial DOS analysis[56] and enabling bonding analysis via the crystal orbital Hamilton population (COHP) method.[52] Gross electron population numbers and the resulting atomic charges according to Mulliken's method[57] were also obtained from LOBSTER analyses, as described in the literature.[58,56]

Impedance Spectroscopy. The entire sample preparation was carried out inside an Ar-filled glovebox (MBraun, O_2 < 1 ppm, H_2O < 1 ppm). The as-prepared $K_2Ge_3As_3$ (**1**) was ground in an agate mortar and then pressed into pellets with a diameter of 6 mm by applying a pressure of 276 MPa at a temperature of 200 °C for approximately 60 min. This was done by a heatable hydraulic press (P/O/Weber, Remshalden, Germany) with polished stainless steel dies. The thickness of the pellets ranged between 0.5 and 1 mm and was determined by a micrometer caliper (Mitutoyo, Neuss, Germany). Platinum electrodes were coated on both faces of the pellets using a sputter coater (108auto, Cressington, Watford, England). To promote good contact between the grains, the pellets were annealed at 200 °C for 24 h within an evacuated silica glass tube. The heating rate was 50 °C, whereas the cooling was not rate-controlled. For the impedance measurements, the pellets were mounted in a home-built, air-tight sample cell in a two-electrode arrangement. Alternating current (AC) impedance data were collected using an Alpha-AK impedance analyzer (Novocontrol, Montabaur, Germany) over a frequency range of 1 MHz−0.1 Hz with an applied root-mean-square AC voltage of 50 mV. The measurements were carried out at temperatures between 0 and 220 °C; the sample temperature was controlled by the Novocontrol Quatro Cryosystem. The maximum temperature variation tolerated during the impedance measurements was ±0.1 K. For the fitting of the obtained spectra, the impedance analysis software RelaxIS (RHD Instruments, Darmstadt, Germany) was used.

RESULTS AND DISCUSSION

Synthesis, Crystal Structure, and Crystal Fiber Separation. Compound **1** is obtained in very good yield (approximately 80% based on Ge) and phase purity, as shown by X-ray powder diffraction (Figure S7). It crystallizes in the orthorhombic space group *Pnnm* (a = 14.1466(7) Å, b = 16.3002(10) Å, and c = 3.7489(2) Å; for details of the structure refinement and crystal data, see Table 1). As reported previously for similar cases,[59] **1** is insoluble, even in highly polar solvents such as 1,2-diaminoethane and liquid ammonia. In this regard, **1** is not likely to act as a direct precursor to the aforementioned binary molecular anions, at least not via reactions in solutions.

Figure 2 illustrates the crystal structure of **1**. The anionic substructure, formally $^1_\infty\{(Ge_3As_3)^{2-}\}$, is based on a complex secondary building unit that is linked into one-dimensional strands extending along the crystallographic c axis. This building unit comprises two identical heteroatomic 9-atom cages, in which one As and two Ge atoms of a six-membered Ge_4As_2 = $As(Ge_2)_2As$ ring are bonded to a capping As_2Ge unit. This cage represents a noradamantane-like architecture, which was described previously also for organogermanium chalcogenide clusters.[60−63] This underlines the applicability of the *pseudo*-element or isolobal concept even in such complicated cases, with Ge replacing C, As or Ge^- replacing CH, and As^- replacing CH_2 of the parent noradamantane molecule (noradamantane = tricyclo[3.3.1.$0^{3,7}$]nonane, C_9H_{14}). It is worth noting that the recently reported structure of K_2TlBi[26] is based on another cage type that is known from organotetrel chalcogenide clusters, namely, the "double-decker"-like architecture,[64−68] which represents an isomeric form of the prominent adamantane unit (adamantane = tricyclo[3.3.1.$1^{3,7}$]-decane, $C_{10}H_{16}$) in such clusters. To form the secondary building unit of **1**, the noradamantane-type cage is linked to a second, identical building unit, which is inverted with respect

DOI: 10.1021/acs.chemmater.9b02827
Chem. Mater. 2019, 31, 8839−8849

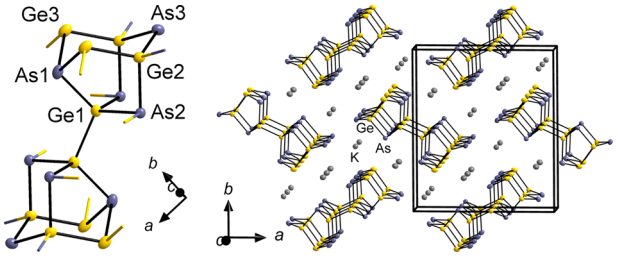

Figure 2. Crystal structure of **1**. Left: close-up of the secondary building unit of the anionic strandlike substructure, consisting of two Ge−Ge-linked noradamantane-like cages; the connection to adjacent building units is illustrated by outgoing two-colored bonds, with the color code reflecting the nature of the involved atom types. Right: view of a section of the crystal structure, viewed approximately along the crystallographic *c* axis. Selected distances (Å): Ge1−As2 2.4328(10), Ge1−As1 2.4795(17), Ge2−Ge3 2.4794(17), Ge2−As2 2.4625(15), Ge2−As3 2.4131(10)−2.4131(1), Ge3−As3 2.4793(12)−2.4794(12), Ge1−Ge1′ 2.447(2).

to the first one. The connection is made via a Ge−Ge bond that comprises an inversion center of the structure (Figure 2, left). The one-dimensional, C_2-symmetric strand along <001> is constructed in that each of the building units shares the atoms Ge2, Ge3, and As2 with its two neighboring building units (Figure 2, right). The bandlike arrangement is slightly inclined by a ± 22.65(1)° rotation about the C_2 axis running along $0,{}^1/_2,c$ and ${}^1/_2,0,c$. The strands are separated from each other by one layer of potassium ions located between the anionic units. The two distinct K^+ ions each possess four closest As atoms within 3.280(3)−3.490(2) Å and one (K1) or two (K2) closest Ge atoms within 3.469(3)−3.654(3) Å. Additionally, one As atom (K1) and/or two Ge atoms (K1/K2) are somewhat farther apart (3.620(3) − 3.784(3) Å); see Figure S2.

The assignment of atom types was done with a combination of micro X-ray fluorescence (μ-XRF) spectroscopy and electronic considerations, as follows. The K:Ge:As composition of 2:3:3 was confirmed by μ-XRF data (see Table S1 and Figure S3). Assuming that the anionic moiety is electron-precise, as typically seen for this kind of *Zintl* phases, it is reasonable to identify all atoms with four bonds as Ge^0 (Ge1, Ge2), the atoms with three bonds as As^0 (As1, As2) or Ge^- (Ge3), and the remaining atom forming two bonds as As^- (As3). This assignment is in agreement with minimal charge accumulation on both types of atoms.

The three-bonded atoms (As1, As2, and Ge3) could generally be of either species, namely, As^0 or Ge^-. However, as the atoms with closest contacts to next K^+ ions should rather be As than Ge, according to the observations made for the related compounds KGe_3As_3[28] and $NaGe_6As_6$,[69] the assignment seems to be reasonable in the given way. Another indication for this is the presence of either isolated Ge atoms or Ge−Ge dumbbells in the structure (see Figure 1, left), such as found for all structures of this type, $LiGe_3As_3$,[70] $BaGe_2As_2$,[71] and $Sr_3Ge_2As_4$,[72] whereas a switch of Ge3 with As1 would produce a Ge_4 chain. However, we would like to suggest that this alternative modification, with inverted assignment of atoms to the Ge3 and As1 positions, may still co-exist in the solid, as the second model is only slightly higher in energy, by 0.015 eV, according to quantum-chemical studies (see below). We attribute this to the following two reasons: First, in both structures, there are two Ge−K distances that are shorter than two of the (closer) As3−K distances (3.490 Å), amounting to 3.469 Å (involving Ge3) in the energetically preferred structure and to 3.431 Å in the alternate version (involving the original As1 position that was switched to Ge3); as reflected by the very slight energy difference, this structural effect is not significant, which can be understood based on the fact that a Ge atom on the As3 position would be (at least partially) negatively charged ("Ge^-"). Second, although none of the related phases quoted above features a Ge_4 chain, this arrangement is not unprecedented in heteroatomic *Zintl*

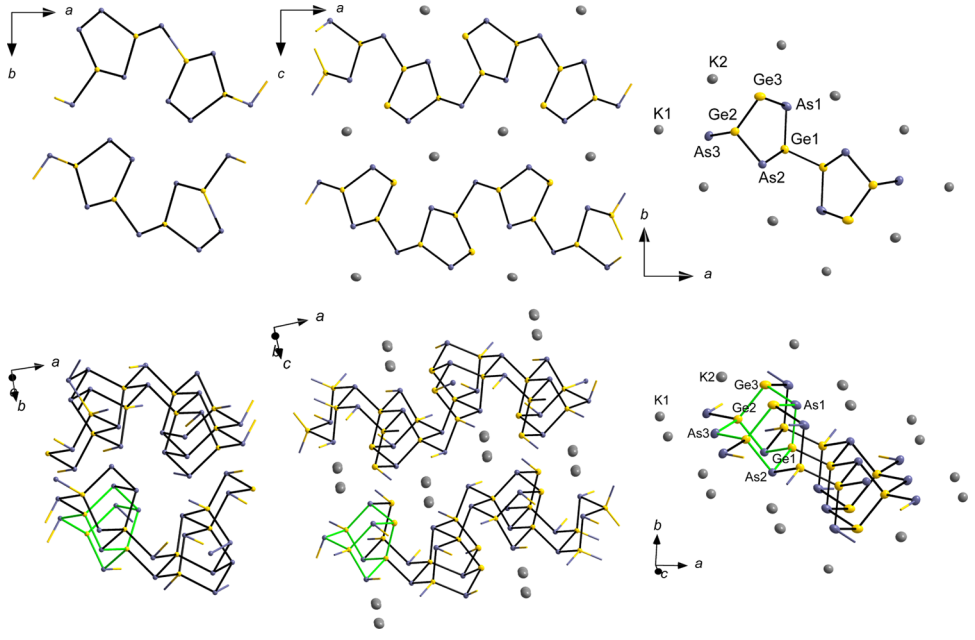

Figure 3. Comparison of the related Ge/As substructures of $GeAs_2$[29,30] (top left, viewed along <001>, and bottom left, slightly rotated), KGe_3As_3[28] (top center, viewed along <010>, and bottom center, slightly rotated), and $K_2Ge_3As_3$ (**1**; top right, viewed along <001>, and bottom right, slightly rotated). One noradamantane-like unit per structure is highlighted by green bonds.

DOI: 10.1021/acs.chemmater.9b02827
Chem. Mater. 2019, 31, 8839−8849

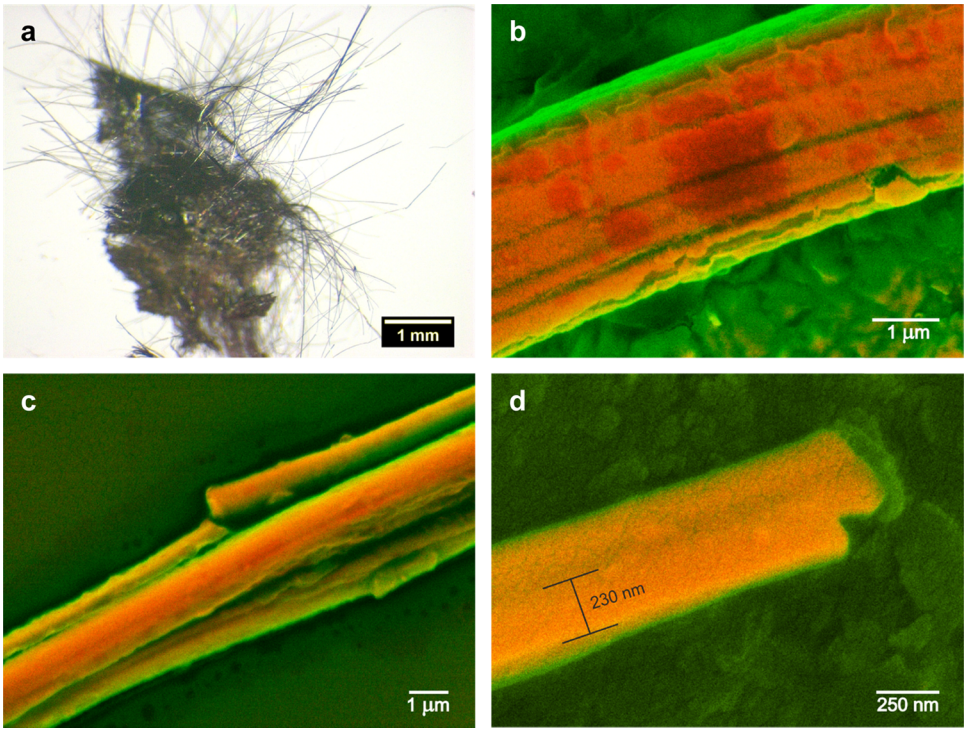

Figure 4. (a) Light-microscopic image of **1** under paraffin oil, indicating its tendency to form agglomerates, from which single-crystalline fibers emerge. (b) Scanning electron microscopic (SEM) image of an untreated isolated fiber of **1**, already indicating the presence of several thinner fibers. (c) SEM images of **1** after ultrasonification for 100 min, showing beginning split up. (d) SEM images of **1** after ultrasonification for 200 min, yielding separated fibers of 0.15−0.5 μm in diameter.

chemistry: indeed, the binary *Zintl* anion $(Ge_4Bi_{14})^{4-}$ contains a Ge_4 chain in each of its three energetically preferred isomers, whereas separation of the atoms leads to higher-energy isomers.[73]

Anyway, both models are in accordance with the sum formula determined by μ-XRF. The two negative charges per formula unit (on Ge3 and As3 in the slightly more stable modification) are balanced by two potassium cations per formula unit. The asymmetric unit comprises one formula unit on special positions, hence with site occupation factors of 0.5 for each of the atoms, with Ge2, Ge3, and As2 being shared between two neighboring cages.

While this one-dimensionally extended motif of linked noradamantane-type cages has not been observed in any other intermetallic phase so far, it is related to the covalently bonded units in the layered structure of $GeAs_2$[29,30] and in the related *Zintl* phase KGe_3As_3.[28] A comparison of these structures with that of compound **1** is provided in Figure 3, with one of the noradamantane units in each of the structures highlighted by green bonds. In $GeAs_2$ (Figure 3, left), the noradamantane-type units are composed of three Ge and six As atoms each, with an As atom located on the corresponding Ge3 site in the noradamantane cage in **1**. Strands of fused noradamantane units that extend parallel to the crystallographic *c* axis are further linked by three-bonded As atoms via Ge−As bonds. Hence, there are exclusively heteroatomic bonds in this binary compound comprising neutral Ge/As layers. Incorporation of 0.5 K atoms per formula unit to $GeAs_2$ causes the formation of an anionic Ge/As substructure. Simultaneously, one quarter of the As atoms are replaced by Ge atoms, yielding $K_{0.5}Ge_{1.5}As_{1.5}$ (i.e., KGe_3As_3; Figure 3, center). This structure contains one homoatomic Ge−Ge bond, yet it still retains the overall layered structure that extends parallel to the *ab* plane in this structure.

Further reduction of the substructure by incorporation of twice the amount of K (formally) yields $K_2Ge_3As_3$ (**1**; Figure 3, right). While the composition and structure of the noradamantane-type cages are identical to those in KGe_3As_3, including the homoatomic Ge1−Ge3 bond, a reduction of the dimensionality of the polyanion takes place toward the one-dimensional Ge/As substructure. However, the latter cannot be derived from the layers discussed above by mere cutting of bonds. Instead, the relative orientation of the adjacent strand of fused noradamantane cages, all of which extend along the <001> direction, is different from that found in the layered structures. Linkage of the two strands into the bandlike one-dimensional substructure does not occur via Ge−As bonds to a three-bonded As atom but by direct Ge−Ge bonds instead (Ge1−Ge1′) upon rotation of one of the two strands about the axis orthogonal to the former layers (i.e., about *b* in $GeAs_2$, about *c* in KGe_3As_3).

The described series of alkali-metal intercalation products is reminiscent of the compound $NaGe_6As_6$,[69] which can be described as stemming from the intercalation of Na ions into GeAs.[31,32] Both solids contain layers of the general formula $^2_\infty\{(Ge_6As_6)^q\}$ (GeAs: $q = 0$; $NaGe_6As_6$: $q = -1$), which are set apart from each other upon intercalation of Na^+ cations. However, as there is no significant structural change within the Ge/As substructure in this case, the reduction of the Ge−As framework relates to n-doping of the substance.

Examples for binary or ternary *Zintl* phases that exhibit one-dimensional anionic substructures are CaSi,[74] APn (A = alkali metal; Pn = P, As),[75−78] K_2TtAs_2 (Tt = Ge, Sn),[27,78] or Ae_3TrPn_3 and $Ae_5Tr_2Pn_6$ (Ae = Ca, Sr, and Ba; Tr = Al, Ga, and In; Pn = P, As, and Sb).[79−81] The nature of these strands

DOI: 10.1021/acs.chemmater.9b02827
Chem. Mater. 2019, 31, 8839−8849

can be very different, ranging from "real" 1D chains of atoms, as found in $^1_\infty\{Si^{2-}\}$ or $^1_\infty\{Pn\}$, that are related to the structures of the elemental semiconductors gray selenium and black tellurium, to pseudo-1D structures that are based on one-dimensionally linked building units. The latter may be tetrahedra, such as those connected in the SiS_2-like structure of $^1_\infty\{(TtAs_2)\}$ or in the diverse substructures of the quoted $Ae_xTr_yPn_z$ phases. In this sense, the substructure of **1** described above is also to be viewed as a pseudo-1D structure, which at the same time belongs to the most complicated ones that have been described to date for *Zintl* phases.

1 forms fine fibers with a metallic luster, which are sensitive toward air and moisture. The fibrous nature of the material can be observed with the naked eye (see Figure 1), but it becomes even more obvious upon inspection of the compound via optical and electron microscopies. Figure 4 provides a light-microscopic image of long single crystals of **1** that grow out of a knot of material (top left) and scanning electron microscopic (SEM) images of these fibers. Under the optical microscope (Figure 4a), the fibers seem to be made up from a single strand. However, when being inspected with a scanning electron microscope, it becomes evident that the fibers consist of thin strands of the material that agglomerate to form the macroscopic fibers (Figure 4b), which readily split up further. This was confirmed by treatment of the material in an ultrasonic bath for several minutes, as illustrated in Figure 4c. This eventually yields separated fibers of 0.15−0.5 μm in diameter (Figure 4d).

Optical Absorption Properties. To gain insight into the electronic properties of compound **1**, we measured its optical absorption behavior by means of the diffuse reflectance method. The UV−vis spectrum is shown in Figure 5. The

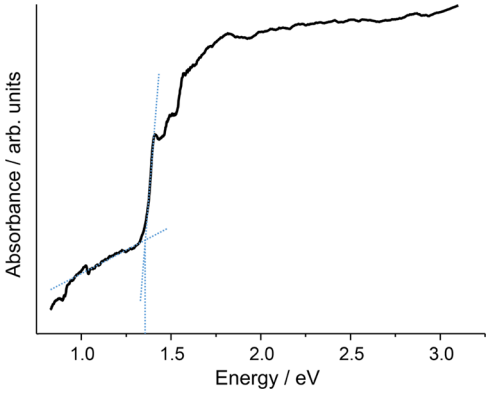

Figure 5. UV−vis spectrum of compound **1**, measured on ground single crystals of the material (solid black line). The onset of absorption was determined by the tangent method (blue lines).

onset of absorption, indicating the lowest possible excitation energy, was determined to occur in the near-infrared, at around 1.37 eV (905 nm). The absorption eventually reaches saturation at about 1.8 eV (690 nm) and covers the whole UV−vis range, which is in agreement with the deeply black appearance of the fibers.

Electronic Structure and Bonding. To gain further insight into the electronic structure and the bonding characteristics of compound **1**, and to further corroborate the experimental findings, quantum-chemical calculations based on density-functional theory were performed, as described in the methodology section. Upon structural optimization, the lattice parameters in the ground state arrive at a = 14.102 Å, b = 16.528 Å, and c = 3.796 Å, in excellent agreement with experimental values, with the largest deviation for b being below 1.5%. For this optimized structural model, Figure 6 shows (a) the resulting band structure and (b) the corresponding total density of states (DOS) with orbital-resolved contributions of the individual atomic species. The band gap obtained from DFT using the SCAN functional is approximately 1.4 eV, in excellent agreement with the experimental data. The positions of the valence band maximum (VB_{max}) and conduction band minimum (CB_{min}) as indicated in the band structure (Figure 6a) indicate a very slight offset of the **k** vector, suggesting that compound **1** is an indirect band-gap material. However, the magnitude of this offset is very small and may be within the margin of error, possibly due to the choice of the **k**-point path through the *Brillouin* zone and the corresponding **k**-point density along the said path. Thus, the *Tauc* formalism was applied to the experimental data of the absorption spectrum, which rather suggests a direct band gap to exist (see Figure S11).

The density of states (DOS) plots (Figure 6b) help in the interpretation of the band structure: the narrow, almost flat band slightly below −14 eV reflects the 3p levels of K exclusively, whereas the region between approx. −13 and −6 eV is dominated by 4s and 4p contributions of Ge and As. In this region, for Ge, the 4s levels are dominant throughout, whereas for As, they are dominant up to −10 eV, with equal contributions of 4s and 4p levels between −10 and −6 eV. The occupied bands between −4 eV and the Fermi level at 0 eV are composed nearly exclusively of 4p levels for both metalloid species. For K, no significant contribution of the 4s valence electrons to the valence band can be observed, in contrast to prominent 4s levels in the unoccupied regions of the band structure above approx. 1.4 eV.

This already underlines the cationic nature of K in this compound, as alluded to in the structural description, based on the examination of the electronic structure as well, and can be reinforced further via the examination of the atomic charges from a Mulliken analysis. These are shown to be approximately 0.05 for the Ge atoms previously identified as neutral Ge1 and Ge2 in Figure 2 and around −0.4 for Ge3, previously identified as anionic, in excellent agreement with assignment of charges given in the structural discussion above. For As, there are two distinct groupings, with charges of approximately −0.28 and −0.36 for As1 and As2, respectively (assigned as As^0 based on the coordination mode), and an average charge of −0.75 for As3 (identified as As^-). The discrepancy between the negative gross Mulliken charges for As1 and As2 and attributing them as neutral atoms based on the threefold coordination are resolved when considering that any quantum-mechanical charge is not equatable with a (highly formal) oxidation number. However, they can and do serve as a qualitative predictor and in this role are indeed in good agreement with the experimental data. Finally, for K, the Mulliken charge is 0.85 on average, in agreement with the cationic character of this atom type in compound **1**. The overall agreement of these data finally corroborates the composition determined by μ-XRF spectroscopy.

The COHP analysis of the bonding characteristics is shown in Figure 7, depicting all contacts between 1 and 5 Å, corresponding to the 1st, 2nd, and 3rd coordination shells (CS) for each species−species interaction, as preceding radial distribution function analyses showed. For homoatomic

DOI: 10.1021/acs.chemmater.9b02827
Chem. Mater. 2019, 31, 8839−8849

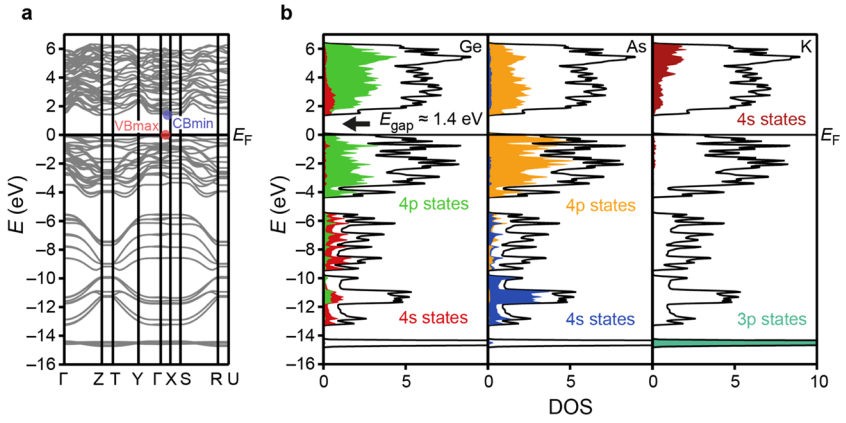

Figure 6. (a) Electronic band structure of **1** with the energetically highest occupied band indicated as the valence band maximum (VBmax, red circle) and the lowest unoccupied band indicated as the conduction band minimum (CBmin, blue circle). (b) Total density of states (DOS) plot of **1** (black line) with individual, orbital-resolved local DOS contributions (filled, colored regions) to the total DOS for each atomic species. The Fermi level (E_F) is set as 0 eV.

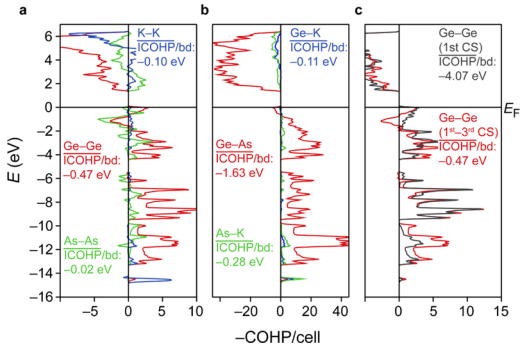

Figure 7. COHP diagrams showing the total interactions per cell for homoatomic (a) and heteroatomic (b) contacts for the 1st, 2nd, and 3rd coordination shells of each atom. The average integrated COHP value for one bond of a given type is indicated as well. A comparison between the six strongest Ge−Ge bonds in the 1st coordination shell (CS) and the sum over all Ge−Ge contacts across all three CS is shown in (c). Energetic scaling (*y*-axis) for all three diagrams is identical, the COHP scaling (*x*-axis) is not. The Fermi level is set to 0 eV.

contacts, i.e., Ge−Ge, As−As, and K−K, it is evident in Figure 7a that the Ge−Ge interactions are the strongest by far, with exclusively bonding characteristics between −14 and −2 eV, exhibiting a small antibonding region close to the Fermi level and then assuming a bonding character directly below the Fermi level again. The average integrated COHP (ICOHP) value of −0.47 eV per bond is nearly five times higher than that of the second-strongest interaction, K−K. For the latter, it is somewhat surprising that a narrow, but significant, bonding peak at around −15 eV is clearly seen, corresponding to the energetic region occupied by the 3p levels and indicating that these have at least some quantifiable impact on interpotassium bonding despite being part of, in the classical picture, a closed and filled shell. However, as the 3s electrons of K are not accounted for in the atomic potential, this is not a "true" noble-gas configuration, and furthermore, the behavior in the solid state is distinct from that of the free gas phase; hence, interactions among these atoms cannot be disregarded a priori. The K−K interactions at higher energies up to the Fermi level are insignificant, unsurprisingly, due to the observed depopulation of the 4s valence levels. Finally, among the homoatomic contacts, As−As interactions are largely negligible based on the average interaction energy per bond (approximately −0.02 eV), but due to the large amount of As−As contacts, there still is an observable total contribution especially in the region beneath the Fermi level. However, there is a notable antibonding component for As−As interactions exceeding that present in the Ge−Ge interactions.

When heteroatomic contacts (shown in Figure 7b) are considered, the interaction between the two metalloids Ge and As proves to be the supremely dominant one. It is the single sstrongest interaction, both summed over the entire examined range per cell and on a per-bond basis, with an average ICOHP of −1.63 eV per bond, more than five times stronger than the next contender As−K. A broad qualitative similarity of the Ge−Ge interaction and the Ge−As interaction can be observed as well upon direct comparison of the two; however, the antibonding region beneath the Fermi level is, relatively speaking, much smaller for Ge−As than it is for Ge−Ge: the Ge−As bond is less destabilized overall. The other two heteroatomic interactions, As−K and Ge−K, are significantly weaker but, remarkably, show no antibonding characteristics at all below the Fermi level, exemplifying that heteroatomic contacts have stronger bonding contributions than homoatomic ones.

Finally, in Figure 7c, the Ge−Ge interaction is examined again, comparing the curve from (a) with interactions in the 1st, 2nd, and 3rd CS to those in the 1st CS exclusively. Although the amount of the latter contacts is only six, as opposed to 58 for the former, their contribution forms half of the total Ge−Ge interactions between −14 and −10 eV and nearly the entire total between −10 and −6 eV. This is reflected in the average ICOHP value of −4.07 eV per bond and the absence of antibonding interactions in the 1st CS, even further demonstrating the strength of the Ge−Ge bond. In light of this analysis, the strength of the qualitatively quite similar Ge−As interaction must be evaluated again, considering solely the 1st CS in this case as well and arriving at an average ICOHP value of −4.14 eV per bond. In contrast to the Ge−Ge interaction, in which there is a qualitative change upon examining the 1st CS only, namely, the vanishing of the antibonding region, there is no change in bonding character for Ge−As. The increase in bond strength is only due to the amount of bonds considered; for this reason, it is not shown separately. Considering these findings, it is clear that the Ge−

DOI: 10.1021/acs.chemmater.9b02827
Chem. Mater. 2019, 31, 8839−8849

As and Ge−Ge contacts exhibit the strongest bonding interactions by far, being responsible for the stability of the present material overall.

To sidestep the so-called "coloring problem"[82] and verify the assignment of the atomic positions, particularly in relation to Ge and As, we have also performed calculations for an alternative structural model of **1**. In this alternative model, the crystal structure itself remains identical, but the Ge3 and As1 positions in the noradamantane-type cage are swapped, as depicted in Figure S8 of the Supporting Information. The structural model obtained from the experiment was both treated in a static calculation and fully structurally optimized. The total energies of both the system as described in the article (**desc**) and the one with alternative Ge3/As1 assignment (**alt**) are very similar for both the static and the optimized case, as seen in Table S2 of the Supporting Information. The described structure is minimally favored energetically; however, the difference of less than 2 kJ/mol is within the accuracy of DFT. Thus, the reassignment of the positions has no significant impact from a purely energetic point of view, surprisingly enough.

Furthermore, the total DOS of the **desc** and **alt** structures were compared, as shown in Figure S9 in the Supporting Information. These are qualitatively and semiquantitatively similar, with very minor changes below the Fermi level. In particular, the band-gap size is 1.4 eV in both cases and thus is entirely unaffected by the Ge3/As1 position exchange. For a comparison of the bonding interactions in **desc** and **alt** via COHP, the differences are more pronounced: while the two strongest interactions, Ge−As and Ge−Ge, show a similar qualitative character throughout the entire energy range, the region immediately below the Fermi level is affected by the position swap, particularly in Ge−Ge, as seen in Figure S10 of the Supporting Information. For both strongest interactions, the averaged ICOHP value per bond at the Fermi level indicates that the bonding character is stronger in the **desc** structure, indicating increased stability. This trend continues for all interactions except Ge−K: their bonding character is either stronger in **desc** or unchanged. For comparison, all ICOHP values are listed in Table S3 in the Supporting Information.

In summary, both the energetic comparison and particularly the bonding analysis indicate the stability of the structure with the described assignment, further backing up the experimental data. While clearly pronounced for the bonding characteristics, the preference is marginal from a purely total-energetic point of view, and the size of the band gap is entirely unaffected by the exchange of the atomic position assignment. Hence, no further variations of position assignment were considered.

In addition, due to the marginal energetic (absolute) difference of approximately 0.015 eV (Table S2), a coexistence of both arrangements due to thermally induced position exchange is highly likely. As the energetic differences are roughly comparable for both the static case (in which the lattice parameters are identical for both arrangements) and the optimized case, it can be assumed that said energy difference is mainly due to the exchange barrier and not structural effects. Under this assumption, for the optimized case, the change in temperature needed to induce a Ge3/As1 position exchange is $T = \frac{\Delta E}{k_B} = 174$ K. This difference refers to the entire unit cell, with position exchanges of four Ge3/As1 pairs. For simplification, energetic equivalence for each exchange due to structural symmetry is further assumed so that the energetic barrier for a single Ge3/As1 pair position exchange is roughly 0.0038 eV, corresponding to a temperature change of approximately 43 K to overcome this barrier. Molecular dynamics or nudged elastic band calculations will yield more realistic values for energetic diffusion barriers; however, in the framework of this study, this approximation is sufficient. Thus, due to standard Boltzmann distribution, it is evident that both structural arrangements (and intermediate forms where not all positions are swapped) are likely to co-exist at room temperature and above, with the described structure predominating both for energetic reasons and due to the described bonding-induced stabilization.

Charge Transport Properties. For elucidation of the charge transport properties, impedance spectra of a pellet of **1** between ion-blocking Pt electrodes were recorded. A Nyquist plot of the impedance (taken at 200 °C) is shown in Figure 8.

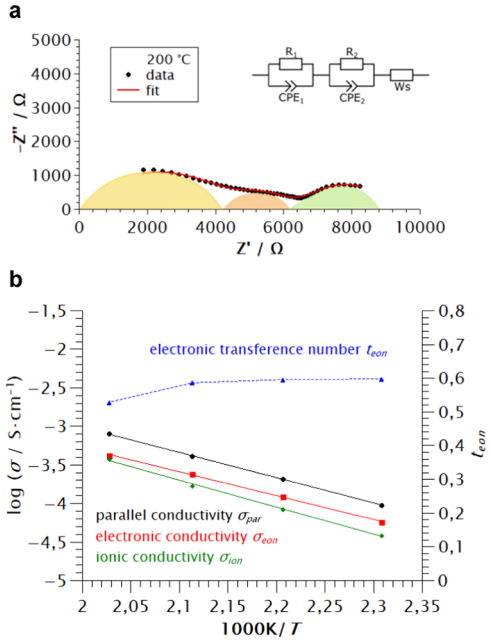

Figure 8. (a) Representative Nyquist plot of the impedance of $K_2Ge_3As_3$ (**1**) at 200 °C. The inset shows the equivalent circuit used for fitting the impedance spectra. (b) Arrhenius plots of the parallel, electronic, and ionic conductivity of **1**. In addition, the electronic transference number is plotted versus the inverse temperature.

In the inset, we sketch the equivalent circuit used for fitting the spectrum. Two R ‖ CPE elements in series were used for fitting the high-frequency and intermediate-frequency part of the spectrum. The impedance of a constant-phase element (CPE) is given by $Z_{CPE} = Q^{-1}(i\omega)^{-\alpha}$ with $\alpha \leq 1$. The capacitance of the respective semicircle can be calculated from the Brug formula $C_i = (Q_i(R_i)^{1-\alpha_i})^{1/\alpha_i}$.[83] Capacitance values around 10^{-10} F cm^{-2} were obtained for the high-frequency semicircle showing that this semicircle is caused by bulk charge transport. Since **1** is a mixed ionic/electronic conductor, the resistances R_1 can be identified with the parallel resistance $R_{par} = (R_{ion}^{-1} + R_{eon}^{-1})^{-1}$, with R_{ion} and R_{eon} denoting the ionic and the electronic resistance, respectively. This is because at high frequencies, ion blocking at the electrodes is negligible; therefore, both ion transport and electron transport in the bulk contribute to the conductivity of the sample. The intermediate-frequency semicircle was characterized by

DOI: 10.1021/acs.chemmater.9b02827
Chem. Mater. 2019, 31, 8839−8849

capacitance values between 10^{-7} and 10^{-6} F cm^{-2}, indicating that this semicircle is caused by the interface between the sample and the Pt electrodes. The low-frequency part of the impedance spectrum was fitted by a Warburg-short element, which describes the formation of K^+/e^- concentration profiles over the bulk of the sample, resulting in a blocking of the K^+ ions and in a purely electronic current at very low frequencies.[84] The Warburg impedance can be written as $Z_{Ws} = R_{Ws}\frac{\tanh((i\omega\tau)^{\alpha})}{(i\omega\tau)^{\alpha}}$ with the Warburg coefficient R_{Ws}, the time constant τ, and the exponent α. The electronic resistance R_{eon} of the sample is then given by $R_1 + R_{Ws}$, i.e., by the low-frequency resistance minus the interfacial resistance R_2. From the obtained ionic and electronic resistances, we calculated the ionic conductivity $\sigma_{ion} = (R_{ion})^{-1}d/A$, the electronic conductivity $\sigma_{eon} = (R_{eon})^{-1}d/A$, and the parallel conductivity of the sample, $\sigma_{par} = ((R_{ion})^{-1} + (R_{eon})^{-1})d/A$. Here, d and A denote the thickness and the area of the sample, respectively.

Figure 8b shows Arrhenius plots of σ_{ion}, σ_{eon}, and σ_{par}. Only data in a temperature range between 160 and 220 °C are shown since at lower temperatures, the Warburg-short behavior at low frequencies was not detectable; therefore, σ_{ion} and σ_{eon} could not be determined. The obtained activation energies are 0.69 eV for the ionic conductivity, 0.61 eV for the electronic conductivity, and 0.65 eV for the parallel conductivity.

Due to the similar activation energies of ionic and electronic conductivities, the electronic transference number $t_{eon} = \frac{\sigma_{eon}}{\sigma_{par}}$ shows only a weak temperature dependence with values between 0.5 and 0.6. The activation energy for the electronic conductivity is close to half the size of the band gap. This indicates that the Fermi level of **1** is roughly in the middle of the band gap and that the electronic conductivity is caused by intrinsic charge carriers. It should be noted that, in contrast, the Fermi level as shown in Figures 6 and 7 is located at the highest occupied band, and thus at the lower edge at the gap, by reasons of the computational convention. However, the gap size is represented accurately, within DFT limits.

Regarding the results of the detailed investigation of the electronic structure that clearly indicated the dominance of Ge−Ge and Ge−As bonding and Ge as well as As contributions to the valence and conduction bands, we assume that the electronic conductivity is mainly due to the extended anionic substructure. However, the question of whether single fibers of **1** show anisotropic conductivity along the strands could not be answered within this study since the corresponding setup is not yet adopted to the demands of the air-sensitive compound. This will be subject to future investigations.

CONCLUSIONS

In summary, we report about the synthesis of a new ternary *Zintl* phase, $K_2Ge_3As_3$, and the thorough investigation of its structural, electronic, bonding, and charge transport properties. Different from known compounds in the system $K_xGe_yAs_z$, the anionic substructure is based on pseudo-one-dimensional strands of the composition $^1_\infty\{(Ge_3As_3)^{2-}\}$. The substructure seems to determine the morphology of the compound, which emerges from the solid-state reaction as bundles of extremely thin fibers that can be separated from each other by ultrasonification. Measurements of the optical absorption behavior and band structure calculations indicate that the compound exhibits a narrow semiconductor-like band gap. In addition, COHP bonding analysis reveals that the Ge−As and Ge−Ge interactions are dominant by far, explaining the stability of both the noradamantane-type cages and the linkage of adjacent strands via Ge−Ge bonds. According to impedance spectra of a polycrystalline sample, the material combines ionic and electronic conductivity properties, which may hint at one-dimensional conductivity along the p-block atom strands. Future work will be dedicated to a detailed study of the anisotropic material properties that result from the discussed combination of electronic and transport features.

ASSOCIATED CONTENT

Supporting Information

The Supporting Information is available free of charge on the ACS Publications website at DOI: 10.1021/acs.chemmater.9b02827.

Synthesis details, single-crystal and powder diffraction data, micro X-ray fluorescence spectroscopy data, thermogravimetric analysis, and differential scanning calorimetry data (PDF)

Crystallographic data of **1** (CIF)

AUTHOR INFORMATION

Corresponding Author

*E-mail: dehnen@chemie.uni-marburg.de.

ORCID

Dimitri Bogdanovski: 0000-0001-8881-0777
Bernhard Roling: 0000-0001-7383-1495
Richard Dronskowski: 0000-0002-1925-9624
Stefanie Dehnen: 0000-0002-1325-9228

Author Contributions

The manuscript was written through contributions of all authors. All authors have given approval to the final version of the manuscript.

Notes

The authors declare no competing financial interest.

ACKNOWLEDGMENTS

This work was supported by the Deutsche Forschungsgemeinschaft (DFG) within the framework of GRK1782. We gratefully acknowledge Shangxin Wei for her help with the ultrasonification experiments, Dr Niels Lichtenberger for his help with powder X-ray diffraction, and Dr Johanna Heine for fruitful discussions regarding optical spectroscopy.

ABBREVIATIONS

TGA	thermogravimetric analysis
DSC	differential scanning calorimetry
μ-XRF	micro X-ray fluorescence spectroscopy
SE	secondary electrons
BE	backscattering electrons
CPE	constant-phase element

REFERENCES

(1) Snyder, G. J.; Toberer, E. S. Complex thermoelectric materials. *Nat. Mater.* **2008**, *7*, 105−114.
(2) Kauzlarich, S. M.; Browna, S. R.; Snyder, G. J. *Zintl* phases for thermoelectric devices. *Dalton Trans.* **2007**, 2099−2107.

DOI: 10.1021/acs.chemmater.9b02827
Chem. Mater. 2019, 31, 8839−8849

(3) Shuai, J.; Mao, J.; Song, S.; Zhang, Q.; Chen, G.; Ren, Z. Recent progress and future challenges on thermoelectric *Zintl* materials. *Mater. Today Phys.* **2017**, *1*, 74−95.
(4) Zhang, J.; Song, L.; Hindborg Pedersen, S.; Yin, H.; Hung, L. T.; Iversen, B. B. Discovery of high-performance low-cost n-type Mg_3Sb_2-based thermoelectric materials with multi-valley conduction bands. *Nat. Commun.* **2016**, *8*, No. 13901.
(5) Grebenkemper, J. H.; Hu, Y.; Barrett, D.; Gogna, P.; Huang, C.-K.; Bux, S. K.; Kauzlarich, S. M. High Temperature Thermoelectric Properties of $Yb_{14}MnSb_{11}$ Prepared from Reaction of MnSb with the Elements. *Chem. Mater.* **2015**, *27*, 5791−5798.
(6) Zevalkink, A.; Zeier, W. G.; Pomrehn, G.; Schechtel, E.; Tremel, W.; Snyder, G. J. Thermoelectric properties of Sr_3GaSb_3—a chain-forming *Zintl* compound. *Energy Environ. Sci.* **2012**, *5*, 9121−9128.
(7) Zevalkink, A.; Toberer, E. S.; Zeier, W.; Flage-Larsen, E.; Snyder, G. J. Ca_3AlSb_3: an inexpensive, non-toxic thermoelectric material for waste heat recovery. *Energy Environ. Sci.* **2011**, *4*, 510−518.
(8) Toberer, E. S.; Zevalkink, A.; Crisosto, N.; Snyder, G. J. The *Zintl* compound $Ca_5Al_2Sb_6$ for low-cost thermoelectric power generation. *Adv. Funct. Mater.* **2010**, *20*, 4375−4380.
(9) Zevalkink, A.; Pomrehn, G. S.; Johnson, S.; Swallow, J.; Gibbs, Z. M.; Snyder, G. J. Influence of the triel elements (M = Al, Ga, In) on the transport properties of $Ca_5M_2Sb_6$ *Zintl* compounds. *Chem. Mater.* **2012**, *24*, 2091−2098.
(10) Brown, S. R.; Kauzlarich, S. M.; Gascoin, F.; Snyder, G. J. $Yb_{14}MnSb_{11}$: New High Efficiency Thermoelectric Material for Power Generation. *Chem. Mater.* **2006**, *18*, 1873−1877.
(11) Chan, J. Y.; Kauzlarich, S. M. Colossal Magnetoresistance in the Transition-Metal *Zintl* Compound $Eu_{14}MnSb_{11}$. *Chem. Mater.* **1997**, *9*, No. 3132.
(12) Goforth, A. M.; Klavins, P.; Fettinger, J. C.; Kauzlarich, S. M. Magnetic Properties and Negative Colossal Magnetoresistance of the Rare Earth *Zintl* phase $EuIn_2As_2$. *Inorg. Chem.* **2008**, *47*, 11048−11056.
(13) Nagamatsu, J.; Nakagawa, N.; Muranaka, T.; Zenitani, Y.; Akimitsu, J. Superconductivity at 39 K in magnesium diboride. *Nature* **2001**, *410*, 63−64.
(14) Deakin, L.; Lam, R.; Marsiglio, F.; Mar, A. Superconductivity in $Ba_2Sn_3Sb_6$ and $SrSn_3Sb_4$. *J. Alloys Compd.* **2002**, *388*, 69−72.
(15) Scharfe, S.; Kraus, F.; Stegmaier, S.; Schier, A.; Fässler, T. F. *Zintl* Ions, Cage Compounds, and Intermetalloid Clusters of Group 14 and Group 15 Elements. *Angew. Chem., Int. Ed.* **2011**, *50*, 3630−3670.
(16) Mitzinger, S.; Guggolz, L.; Massa, W.; Dehnen, S. Evidence for the Existence of $(SiP_6H_2)^{2-}$ and its Homologs as Examples of Binary Nortricyclane-Type *Zintl* Anions. *Z. Anorg. Allg. Chem.* **2019**, *645*, 153−157.
(17) Mitzinger, S.; Bandemehr, J.; Reiter, K.; McIndoe, J. S.; Xie, X.; Weigend, F.; Corrigan, J. F.; Dehnen, S. $Ge_2P_2)^{2-}$: a binary analogue of P_4 as a precursor to the ternary cluster anion $[Cd_3(Ge_3P)_3]^{3-}$. *Chem. Commun.* **2018**, *54*, 1421−1424.
(18) Mitzinger, S.; Broeckaert, L.; Massa, W.; Weigend, F.; Dehnen, S. Understanding of multimetallic cluster growth. *Nat. Commun.* **2016**, *7*, No. 10480.
(19) Wilson, R. J.; Broeckaert, L.; Spitzer, F.; Weigend, F.; Dehnen, S. $\{[CuSn_5Sb_3]^{2-}\}_2$: A Dimer of Inhomogeneous Superatoms. *Angew. Chem., Int. Ed.* **2016**, *55*, 11775−11780.
(20) Ababei, R.; Heine, J.; Hołynska, M.; Thiele, G.; Weinert, B.; Xie, X.; Weigend, F.; Dehnen, S. Making practical use of the pseudo-element concept: an efficient way to ternary intermetalloid clusters by an isoelectronic Pb^-−Bi combination. *Chem. Commun.* **2012**, *48*, 11295−11297.
(21) Wilson, R. J.; Lichtenberger, N.; Weinert, B.; Dehnen, S. Intermetalloid and Heterometallic Clusters Combining p-Block (Semi)Metals with d- or f-Block Metals. *Chem. Rev.* **2019**, No. 658.
(22) Weinert, B.; Dehnen, S. Binary and Ternary Intermetalloid Clusters. In *Clusters − Contemporary Insight in Structure and Bonding. Structure and Bonding*; Dehnen, S., Ed.; Springer: Cham, Switzerland, 2017; Vol. *174*, pp 99−134
(23) Weinert, B.; Mitzinger, S.; Dehnen, S. (Multi-)Metallic Cluster Growth. *Chem. - Eur. J.* **2018**, *24*, 8470−8490.
(24) Wilson, R. J.; Weinert, B.; Dehnen, S. Recent developments in *Zintl* cluster chemistry. *Dalton Trans.* **2018**, *47*, 14861−14869.
(25) Mayer, K.; Weßing, J.; Fässler, T. F.; Fischer, R. A. Intermetalloid Clusters: Molecules and Solids in a Dialogue. *Angew. Chem., Int. Ed.* **2018**, *57*, 14372−14393.
(26) Lichtenberger, N.; Franzke, Y. J.; Massa, W.; Weigend, F.; Dehnen, S. The Identity of "Ternary" A/Tl/Pb or K/Tl/Bi Solid Mixtures and Binary *Zintl* Anions Isolated From Their Solutions. *Chem. - Eur. J.* **2018**, *24*, 12022−12030.
(27) Eisenmann, B.; Klein, J. SiS_2-isostrukturelle Anionen $[SiP_2^{2-}]$, $[GeAs_2^{2-}]$ und $[SnAs_2^{2-}]$ in Alkaliverbindungen. *J. Less-Common Met.* **1991**, *175*, 109−117.
(28) Khatun, M.; Stoyko, S. S.; Mar, A. Ternary arsenides ATt_3As_3 (A = K, Rb; Tt = Ge, Sn) with layered structures. *J. Solid State Chem.* **2016**, *238*, 229−235.
(29) Bryden, J. H. The Crystal Structures of the Germanium-Arsenic Compounds. I. Germanium Diarsenide. *Acta Crystallogr.* **1962**, *15*, 167−171.
(30) Zhao, T.; Sun, Y.; Shuai, Z.; Wang, D. $GeAs_2$: A IV−V Group Two-Dimensional Semiconductor with Ultralow Thermal Conductivity and High Thermoelectric Efficiency. *Chem. Mater.* **2017**, *29*, 6261−6268.
(31) Stöhr, H.; Klemm, W. Über Zweistoffsysteme mit Germanium. II. Germanium/Arsen, Germanium/Antimon, Germanium/Wismut. *Z. Anorg. Allg. Chem.* **1940**, *244*, 205−223.
(32) Schubert, K.; Dörre, E.; Günzel, E. Kristallchemische Ergebnisse an Phasen aus B-Elementen. *Naturwissenschaften* **1954**, *41*, No. 448.
(33) Ponou, S.; Fässler, T. F. Crystal Growth and Structure Refinement of K_4Ge_9. *Z. Anorg. Allg. Chem.* **2007**, *633*, 393−397.
(34) Emmerling, F.; Röhr, C. Alkaline Metal Arsenides A_3As_7 and AAs (A = K, Rb, Cs). Preparation, Crystal Structure, Vibrational Spectroscopy. *Z. Naturforsch., B* **2002**, *57*, 963−975.
(35) von Schnering, H. G.; Somer, M.; Kliche, G.; Hönle, W.; Meyer, T.; Wolf, J.; Ohse, L.; Kempa, P. B. Chemie und Strukturchemie von Phosphiden und Polyphosphiden. 53. Darstellung, Eigenschaften und Schwingungsspektren der Käfiganionen P_{11}^{3-} und As_{11}^{3-}. *Z. Anorg. Allg. Chem.* **1991**, *601*, 13−30.
(36) Sheldrick, G. M. SHELXT—Integrated space-group and crystal-structure determination. *Acta Crystallogr., Sect. A: Found. Adv.* **2015**, *71*, 3−8.
(37) Sheldrick, G. M. Crystal structure refinement with SHELXL. *Acta Crystallogr., Sect. C: Struct. Chem.* **2015**, *71*, 3−8.
(38) Boldish, S. I.; White, W. B. Optical band gaps of selected ternary sulfide minerals. *Am. Mineral.* **1998**, *83*, 865−871.
(39) Kresse, G.; Hafner, J. Ab initio molecular dynamics for liquid metals. *Phys. Rev. B* **1993**, *47*, 558−561.
(40) Kresse, G.; Hafner, J. Ab initio molecular-dynamics simulation of the liquid-metal–amorphous-semiconductor transition in germanium. *Phys. Rev. B* **1994**, *49*, 14251−14269.
(41) Kresse, G.; Furthmüller, J. Efficiency of ab-initio total energy calculations for metals and semiconductors using a plane-wave basis set. *Comput. Mater. Sci.* **1996**, *6*, 15−50.
(42) Kresse, G.; Furthmüller, J. Efficient iterative schemes for ab initio total-energy calculations using a plane-wave basis set. *Phys. Rev. B* **1996**, *54*, 11169−11186.
(43) Blöchl, P. E. Projector augmented-wave method. *Phys. Rev. B* **1994**, *50*, 17953−17979.
(44) Kresse, G.; Joubert, D. From ultrasoft pseudopotentials to the projector augmented-wave method. *Phys. Rev. B* **1999**, *59*, 1758−1775.
(45) Perdew, J. P.; Burke, K.; Ernzerhof, M. Generalized Gradient Approximation Made Simple. *Phys. Rev. Lett.* **1996**, *77*, 3865−3868.
(46) Blöchl, P. E.; Jepsen, O.; Andersen, O. K. Improved tetrahedron method for Brillouin-zone integrations. *Phys. Rev. B* **1994**, *49*, 16223−16233.

DOI: 10.1021/acs.chemmater.9b02827
Chem. Mater. 2019, 31, 8839−8849

(47) Perdew, J. P.; Levy, M. Physical Content of the Exact Kohn-Sham Orbital Energies: Band Gaps and Derivative Discontinuities. *Phys. Rev. Lett.* **1983**, *51*, 1884−1887.
(48) Perdew, J. P. Density functional theory and the band gap problem. *Int. J. Quantum Chem.* **1985**, *28*, 497−523.
(49) Sham, L. J.; Schlüter, M. Density-Functional Theory of the Energy Gap. *Phys. Rev. Lett.* **1983**, *51*, 1888−1891.
(50) Sun, J.; Ruzsinszky, A.; Perdew, J. P. Strongly Constrained and Appropriately Normed Semilocal Density Functional. *Phys. Rev. Lett.* **2015**, *115*, No. 036402.
(51) Sun, J.; Remsing, R. C.; Zhang, Y.; Sun, Z.; Ruzsinszky, A.; Peng, H.; Yang, Z.; Paul, A.; Waghmare, U.; Wu, X.; Klein, M. L.; Perdew, J. P. Accurate first-principles structures and energies of diversely bonded systems from an efficient density functional. *Nat. Chem.* **2016**, *8*, No. 831.
(52) Dronskowski, R.; Blöchl, P. E. Crystal orbital Hamilton populations (COHP): energy-resolved visualization of chemical bonding in solids based on density-functional calculations. *J. Phys. Chem. A* **1993**, *97*, 8617−8624.
(53) Deringer, V. L.; Tchougréeff, A. L.; Dronskowski, R. Crystal Orbital Hamilton Population (COHP) Analysis As Projected from Plane-Wave Basis Sets. *J. Phys. Chem. A* **2011**, *115*, 5461−5466.
(54) Maintz, S.; Deringer, V. L.; Tchougréeff, A. L.; Dronskowski, R. Analytic projection from plane-wave and PAW wavefunctions and application to chemical-bonding analysis in solids. *J. Comput. Chem.* **2013**, *34*, 2557−2567.
(55) Maintz, S.; Deringer, V. L.; Tchougréeff, A. L.; Dronskowski, R. LOBSTER: A tool to extract chemical bonding from plane-wave based DFT. *J. Comput. Chem.* **2016**, *37*, 1030−1035.
(56) Konze, P. M.; Dronskowski, R.; Deringer, V. L. Exploring Chemical Bonding in Phase-Change Materials with Orbital-Based Indicators. *Phys. Status Solidi RRL* **2019**, *13*, No. 1800579.
(57) Mulliken, R. S. Electronic Population Analysis on LCAO-MO Molecular Wave Functions. I. *J. Chem. Phys.* **1955**, *23*, 1833−1840.
(58) Ertural, C.; Steinberg, S.; Dronskowski, R. Development of a robust tool to extract Mulliken and Löwdin charges from plane waves and its application to solid-state materials. *RSC Adv.* **2019**, *9*, 29821−29830.
(59) Birdwhistell, T. L. T.; Stevens, E. D.; O'Connor, C. J. Synthesis and crystal structure of a novel layered *Zintl* phase: potassium gallium arsenide (59). *Inorg. Chem.* **1990**, *29*, 3892−3894.
(60) Herzog, U.; Borrmann, H. Heteronoradamantanes $Me_2Si_2(RM)_2E_5$ (RM = MeGe, PhSn; E = S, Se). *J. Organomet. Chem.* **2003**, *675*, 42−47.
(61) Heimann, S.; Thiele, G.; Dehnen, S. Nitrile functionalized organogermane chalcogenide clusters with hetero-(nor-)adamantane cores. *J. Organomet. Chem.* **2016**, *813*, 36−40.
(62) Heimann, S.; Hołynska, M.; Dehnen, S. Synthesis, Structures, and Light-Induced Transformation of Keto-Functionalized Selenidogermanate Complexes. *Z. Anorg. Allg. Chem.* **2012**, *638*, 1663−1666.
(63) Heimann, S.; Hołynska, M.; Dehnen, S. In situ Ge−Ge bond formation under ambient conditions: synthesis, characterization and reactivity of organo-functionalized telluridogermanate complexes. *Chem. Commun.* **2011**, *47*, 1881−1883.
(64) Ando, W.; Kadowaki, T.; Kabe, Y.; Ishii, M. A Germanium Sesquisulfide, $(t\mathrm{BuGe})_4S_6$, without Adamantane Structure. *Angew. Chem., Int. Ed.* **1992**, *31*, 59−61.
(65) Unno, M.; Kawai, Y.; Shioyama, H.; Matsumoto, H. Syntheses, Structures, and Properties of Tricyclo[5.1.1.$1^{3,5}$]-tetrasilachalcogenanes $(Thex_2Si_2E_2)E_2$ (E = S, Se) and Tricyclo-[5.1.1.$1^{3,5}$]tetragermachalcogenanes $(Thex_2Ge_2E_2)E_2$ (E = S, Se). *Organometallics* **1997**, *16*, No. 4428.
(66) Varga, R. A.; Silvestru, C. Tetrakis[2-(dimethylaminomethyl)-phenyl]- 1κC,2κC,3κC,4κC-hexa-μ-sulfido1:2κ^4S:S; 1,4κ^2S:S;2:3κ^2S:S;3:4κ^4S:S-tetratin(IV) chloroform solvate. *Acta Crystallogr., Sect. E: Struct. Rep. Online* **2007**, *63*, m2789.
(67) Hassanzadeh Fard, Z.; Xiong, L.; Müller, C.; Hołyńska, M.; Dehnen, S. Synthesis and Reactivity of Functionalized Binary and Ternary Thiometallate Complexes $[(RT)_4S_6]$, $[(RSn)_3S_4]^{2-}$, $[(RT)_2(CuPPh_3)_6S_6]$, and $[(RSn)_6(OMe)_6Cu_2S_6]^{4-}$ (R=C_2H_4COOH, CMe_2CH_2COMe; T=Ge, Sn). *Chem. - Eur. J.* **2009**, *15*, 6595−6604.
(68) Hassanzadeh Fard, Z.; Müller, C.; Harmening, T.; Pöttgen, R.; Dehnen, S. Thiostannate Tin-Tin Bond Formation in Solution: In Situ Generation of the Mixed-Valent, Functionalized Complex $[\{(RSn^{IV})_2(\mu\text{-}S)_2\}_3Sn_2^{III}S_6]$. *Angew. Chem., Int. Ed.* **2009**, *48*, 4441−4444.
(69) Khatun, M.; Mar, A. $NaGe_6As_6$: Insertion of sodium into the layered semiconductor germanium arsenide GeAs. *Z. Naturforsch., B* **2016**, *71*, 375−380.
(70) Mark, J.; Hanrahan, M. P.; Woo, K. E.; Lee, S.; Rossini, A. J.; Kovnir, K. Chemical and Electrochemical Lithiation of van der Waals Tetrel Arsenides. *Chem. - Eur. J.* **2019**, *25*, 6392−6401.
(71) Eisenmann, B.; Schäfer, H. Zintlphasen mit binären Anionen: Zur Kenntnis von $BaGe_2P_2$ und $BaGe_2As_2$. *Z. Naturforsch., B* **1981**, *3*, 415−419.
(72) Eisenmann, B.; Schäfer, H. *Zintl* Phases with Complex Anions: $Sr_3Si_2As_4$ and $Sr_3Ge_2As_4$. *Angew. Chem., Int. Ed.* **1980**, *19*, 490−491.
(73) Wilson, R. J.; Dehnen, S. $(Ge_4Bi_{14})^{4-}$: A Case of Element Segregation on the Molecular Level. *Angew. Chem., Int. Ed.* **2017**, *56*, 3098−3102.
(74) Hellner, E. Die Kristallstruktur des CaSi. *Z. Anorg. Allg. Chem.* **1950**, *261*, 226−236.
(75) Cromer, D. T. The Crystal Structure of LiAs. *Acta Crystallogr.* **1959**, *12*, 36−41.
(76) Hönle, W.; von Schnering, H. G. The Structure of I/V Compounds and Their Relationships. *Acta Crystallogr., Sect. A* **1978**, *34*, S152−S156.
(77) von Schnering, H. G.; Hönle, W. Zur Chemie und Strukturchemie der Phosphide und Polyphosphide. 20. Darstellung, Struktur und Eigenschaften der Alkalimetallmonophosphide NaP und KP. *Z. Anorg. Allg. Chem.* **1979**, *456*, 194−206.
(78) Burtzlaff, S.; Hołyńska, M.; Dehnen, S. Synthesis and Crystal Structures of K_2SnAs_2 and a New Modification of NaAs. *Z. Anorg. Allg. Chem.* **2010**, *636*, 1691−1693.
(79) Cordier, G.; Schäfer, H.; Stelter, M. Sr_3GaSb_3 und Sr_3InP_3, zwei neue Zintlphasen mit komplexen Anionen. *Z. Naturforsch., B: Anorg. Chem., Org. Chem.* **1987**, *42*, 1268−1272.
(80) Cordier, G.; H. Schäfer, H.; Stelter, M. Ca_3AlSb_3 und $Ca_5Al_2Bi_6$ zwei neue Zintlphasen mit kettenförmigen Anionen. *Z. Naturforsch., B: Anorg. Chem., Org. Chem.* **1984**, *39*, 727−732.
(81) Cordier, G.; Czech, E.; Jakowski, M.; Schäfer, H. *Zintl* phases of complex ions-information on $Ca_5Al_2Sb_6$ and $Ca_3Al_2As_4$. *Rev. Chim. Miner* **1981**, *18*, No. 9.
(82) Miller, G. J. The "Coloring Problem" in Solids: How It Affects Structure, Composition and Properties. *Eur. J. Inorg. Chem.* **1998**, *1998*, 523−536.
(83) Brug, G. J.; van den Eeden, A. L. G.; Sluyters-Rehbach, M.; Sluyters, J. H. The Analysis of Electrode Impedances complicated by the Presence of Constant-Phase Element. *J. Electroanal. Chem.* **1984**, *176*, 275−295.
(84) Jamnik, J.; Maier, J.; Pejovnik, S. A powerful electrical network model for the impedance of mixed conductors. *Electrochim. Acta* **1999**, *44*, 4139−4145.

DOI: 10.1021/acs.chemmater.9b02827
Chem. Mater. 2019, 31, 8839−8849